nature communications

Article

https://doi.org/10.1038/s41467-024-55000-8

Amorphous organic-hybrid vanadium oxide for near-barrier-free ultrafast-charging aqueous zinc-ion battery

Received: 20 November 2023

Accepted: 26 November 2024

Published online: 30 December 2024

Check for updates

Mingzhuang Liu[1], Xinghua Li[1] ✉, Mengxia Cui[1], Feiyu Chen[1], Jiaxing Li[1], Weijian Shi[1], Yu Liu[1], Xiaowei Li[1], Yan Wang[2], Wei Zhang[2], Changlu Shao[1] ✉ & Yichun Liu[1] ✉

Fast-charging metal-ion batteries are essential for advancing energy storage technologies, but their performance is often limited by the high activation energy (E_a) required for ion diffusion in solids. Addressing this challenge has been particularly difficult for multivalent ions like Zn^{2+}. Here, we present an amorphous organic-hybrid vanadium oxide (AOH-VO), featuring one-dimensional chains arranged in a disordered structure with atomic/molecular-level pores for promoting hierarchical ion diffusion pathways and reducing Zn^{2+} interactions with the solid skeleton. AOH-VO cathode demonstrates an exceptionally low E_a of 7.8 kJ·mol^{-1} for Zn^{2+} diffusion in solids and 6.3 kJ·mol^{-1} across the cathode-electrolyte interface, both significantly lower than that of electrolyte (13.2 kJ·mol^{-1}) in zinc ion battery. This enables ultrafast charge-discharge performance, with an Ah-level pouch cell achieving 81.3% of its capacity in just 9.5 minutes and retaining 90.7% capacity over 5000 cycles. These findings provide a promising pathway toward stable, ultrafast-charging battery technologies with near-barrier-free ion dynamics.

Ultrafast-charging batteries with robust long-term cycle stability are crucial for applications such as electric vehicles, grid-scale energy storage, and portable electronics[1,2]. Among the potential candidates, aqueous zinc-ion batteries (AZIBs) stand out due to their high energy density, affordability, and nonflammability, bolstered by the superior ion conductivity of their aqueous electrolyte (up to 1 S cm^{-1} vs. non-aqueous electrolytes approximately 1–10 mS cm^{-1})[3,4]. However, achieving ultrafast-charging capabilities in AZIBs remains challenging due to the high activation energy (E_a) associated with metal ion diffusion within active materials and the charge transfer kinetics at the solid-electrolyte interfaces. Despite the excellent metal ion transport in the aqueous electrolyte, these intrinsic barriers hinder overall performance[5].

Zn^{2+} ions, in particular, face significant diffusion challenges within solid materials due to their strong interaction with the solid matrix, resulting in large energy barriers (E_b) for ion hopping between lattice sites[6,7]. Traditional methods to lower E_a or E_b in inorganic materials, such as channel construction, doping, and defect engineering, often induce phase transformations or instabilities, potentially compromising long-term cycle stability[8–10]. Although organic polymers offer stability, their limited capacity hinders their effectiveness in battery applications[11]. Hybrid materials, combining organic molecules with inorganic oxides, can promote stability; however, steric hindrance effects remain a concern for ion migration kinetics[12–14].

Building on the foundational work in amorphous oxides, which demonstrated that lattice disorder can create diffusion paths with reduced E_b[15,16], we hypothesize that amorphous organic-hybrid metal oxides could integrate the benefits of organic-inorganic hybrids while mitigating steric hindrance effects. Unlike crystalline oxides, the random packing of larger organic-hybrid building blocks can form numerous atomic/molecular-level pores, enlarging ion diffusion channels and reducing ion-host material interactions, thereby

[1]Key Laboratory of UV Light-Emitting Materials and Technology of Ministry of Education, Northeast Normal University, Changchun 130024, China. [2]Electron Microscopy Center, Jilin University, Changchun 130012, China. ✉e-mail: lixh781@nenu.edu.cn; clshao@nenu.edu.cn; ycliu@nenu.edu.cn

lowering E_b and enhancing long-term cycle stability. Furthermore, these open pores can fully expose active sites to the electrolyte, enabling fast surface-dominated charge transfer reactions. Despite their potential, amorphous organic-hybrid materials remain underexplored in ultrafast-charging battery applications.

Here, we report an innovative amorphous organic-hybrid vanadium oxide (AOH-VO) for ultrafast-charging AZIBs. AOH-VO features a unique three-dimensional open hollow nanosheet structure formed by the random assembly of one-dimensional (1D) polymer-like organic-hybrid vanadium oxide chains. This configuration creates atomic/molecular-level micropores and multiscale hierarchical ion diffusion pathways, significantly reducing Zn^{2+} ion interaction with the solid skeleton and producing an exceptionally low E_a of 7.8 kJ mol^{-1} (0.081 eV). Our strategy significantly narrows the diffusion coefficient (D_O) gap between solid and electrolyte, offering a threefold reduction in E_a and a three-order of magnitude increase in D_O compared to crystalline counterparts. Furthermore, the weak Zn^{2+}-host interaction enhances stability, enabling over 17,000 cycles at 100 A g^{-1}. This amorphous organic-hybrid metal oxide with disordered 1D-chain structures opens promising avenues for advanced ultrafast-charging metal ion batteries.

Results and discussion

Transformation from crystalline VEG to amorphous AOH-VO

Vanadyl ethylene glycolate (VEG), first reported by Whittingham et al.[17] in 2003, was used as the crystalline organic-hybrid vanadium oxide framework. It has typical 1D structural units periodically arranged like a two-dimensional (2D) centered rectangular structure (Fig. 1a and insets in Fig. 1b). The organic groups (-OCH_2CH_2O-) as chelating ligands coordinate the 1D edge-sharing VO_5 forming parallel alternating serrations. This organic hybridization confers stability to the 1D-VO_5 units. The X-ray diffraction (XRD) peaks of synthesized crystalline VEG (Fig. 1b) exactly match the JCPDS file No. 49-2497 with monoclinic structure[18].

We adopted hydrogen peroxide (H_2O_2) as a regulator for accelerating the reaction rate to transform from crystalline VEG to amorphous AOH-VO (Fig. 1c). The effect of H_2O_2 on crystallinity and local structure can be found in Supplementary Note 1, Supplementary Table 1 and Supplementary Figs. 1–3. The XRD spectrum of AOH-VO (Fig. 1d) shows broad peaks in the 5-80 degrees range, indicating its amorphous nature. The comparison on the Fourier transform infrared (FT-IR) spectra of crystalline VEG and AOH-VO (Fig. 1e) confirm that they have similar characteristic vibrations from the edge-sharing VO_5 (square pyramids structure) and the (-OCH_2CH_2O-) chelating ligands (EG-CL). The EG-CL provides some solubility of in organic solvents similar to organic-polymer chains but different from crystalline and amorphous vanadium oxides (Supplementary Fig. 4). Thermogravimetry coupled mass (TG-MS) spectra of AOH-VO performed under an argon atmosphere (Supplementary Fig. 5) show peak signals near 300 °C for mass-to-charge ratios of 12, 14, and 27, attributed to the decomposition products of C_xH_y. This finding provides additional confirmation of the organic hybridization of AOH-VO.

Thermogravimetric (TG) analysis in air (Fig. 1f and Supplementary Fig. 6a) suggested that the EG-CL-related weight loss of AOH-VO is significantly reduced to 12.45% compared to that of crystalline VEG, i.e., 28.4% which is consistent with the theoretical value[19]. Detailed calculations show that the EG-CL mass ratio in VEG (29.1%) is about twice that in AOH-VO (14.3%), after accounting for adsorbed water (Supplementary Note 2). Meanwhile, V content increasing from 39.77% in VEG to 41.63% in AOH-VO measured by inductively coupled plasma optical emission spectrometry (ICP-OES) also consists of the decreased organic contents in AOH-VO (Supplementary Table 2). Additionally, the differential thermal analysis (DTA) shows that the transformation from the sharp peak of VEG to the broad peak of AOH-VO further supports the transformation from crystalline to amorphous organic-hybrid vanadium oxide with 1D defective EG-chelated VO_5 chains (1D-D-VO_5) (Fig. 1g and Supplementary Fig. 6b).

Density functional theory (DFT) simulation presents the broader and longer V-O bond lengths distribution in the 1D-D-VO_5 structure compared to perfect 1D-VO_5 indicating that V-O bond interactions are sensitive to the atomic local environment (Supplementary Fig. 7 and Supplementary Table 3). These simulation results align with the significant redshift and peak broadening observed in the FT-IR spectra for the V-O and V-O-V bonds in AOH-VO, providing further evidence that AOH-VO, as an amorphous organic hybrid vanadium oxide, contains randomly packed 1D-D-VO_5 units with defective EG-CL and reduced chain-chain interactions.

Moreover, the charge density difference diagram suggest that EG-CL defects can affect chemical states of vanadium element (Fig. 1c). X-ray photoelectron spectroscopy (XPS) revealed that VEG is dominated by V^{4+} and exhibits a 0.46% mass increase due to V^{4+} oxidation to V^{5+} during TG analysis in air, while AOH-VO presents a smaller mass increase, consistent with its mixed V^{5+}/V^{4+} peaks in the XPS spectra (Supplementary Fig. 8). Furthermore, AOH-VO-300 was obtained by calcining AOH-VO samples at 300 °C. The comparative study on FT-IR and XRD spectra (Supplementary Fig. 9a–c) suggests that the local structure of AOH-VO-300 contracts after removing EG-CL, leading to narrower ion transport channels in the amorphous vanadium oxide. Therefore, EG-CL in AOH-VO could stabilize larger ion transport channels than in amorphous vanadium oxide alone. The mixed vanadium chemical states also affect the electronic states of VEG, AOH-VO, AOH-VO-300, and crystalline V_2O_5, as evidenced by the absorption spectra (Supplementary Fig. 10).

Figure 1h shows the V K-edge X-ray absorption near edge structure (XANES) spectra of VEG, AOH-VO, and AOH-VO-300, along with standard V_2O_5 (crystalline) and vanadium foil as reference. The pre-edge peak (denoted as A) originates from the dipole-forbidden (1s → 3d) transition, which becomes dipole-allowed due to the overlap of metal 3d and ligand 2p orbitals as the site symmetry around V decreases[20]. The B peak in the XANES spectra corresponds to the dipole-allowed 1s → 4p transition with a shakedown transition shoulder. Features beyond the 1s → 4p transition, labeled C, arise from transitions to higher np states, resonances, and/or multiple scattering events[20,21].

Compared to vanadium foil, standard V_2O_5 shows a strong A peak due to its asymmetric VO_5-unit structure. AOH-VO and VEG both have stronger A peaks than amorphous AOH-VO-300 and standard V_2O_5, suggesting that EG-CL in the organic-inorganic hybrids enhances the atomic localized asymmetry of VO_5 unit more effectively. Furthermore, the amorphous effect also enlarged the asymmetry of VO_5 unit because AOH-VO and AOH-VO-300 have more intense A-peaks than VEG and standard V_2O_5, respectively.

The A-peak position and absorption edge shift to higher energies from vanadium foil to VEG, AOH-VO, and AOH-VO-300, indicating V^{4+} in VEG, mixed V^{4+}/V^{5+} in AOH-VO, and predominantly V^{5+} in AOH-VO-300. The B and C peaks of AOH-VO-300 align closely with standard V_2O_5, confirming the presence of similar V^{5+} in VO_5 units. In contrast, the B and C peaks of VEG shift to lower energies relative to AOH-VO-300, which is consistent with the lower V^{4+} valence state in VO_5 units with EG-CL. The presence of both B peaks from VEG and AOH-VO-300 in the XANES spectrum of AOH-VO confirms the coexistence of V^{5+} in VO_5 units without EG-CL and V^{4+} in VO_5 units with EG-CL. The broad C peak in AOH-VO is also due to a mix of VO_5 units with and without EG-CL.

Figure 1i, j shows the k^3-weighted, phase-uncorrected Fourier-transformed extended X-ray absorption fine structure (FT-EXAFS) spectra and the wavelet-transform (WT) of the k^3-weighted EXAFS (WT-EXAFS) spectra. Both FT-EXAFS and WT-EXAFS spectra of these samples show peaks at 1–2 Å and 2.5–3 Å, corresponding to V-O and V-V interactions, respectively. VEG and AOH-VO, as organic-inorganic

https://doi.org/10.1038/s41467-024-55000-8

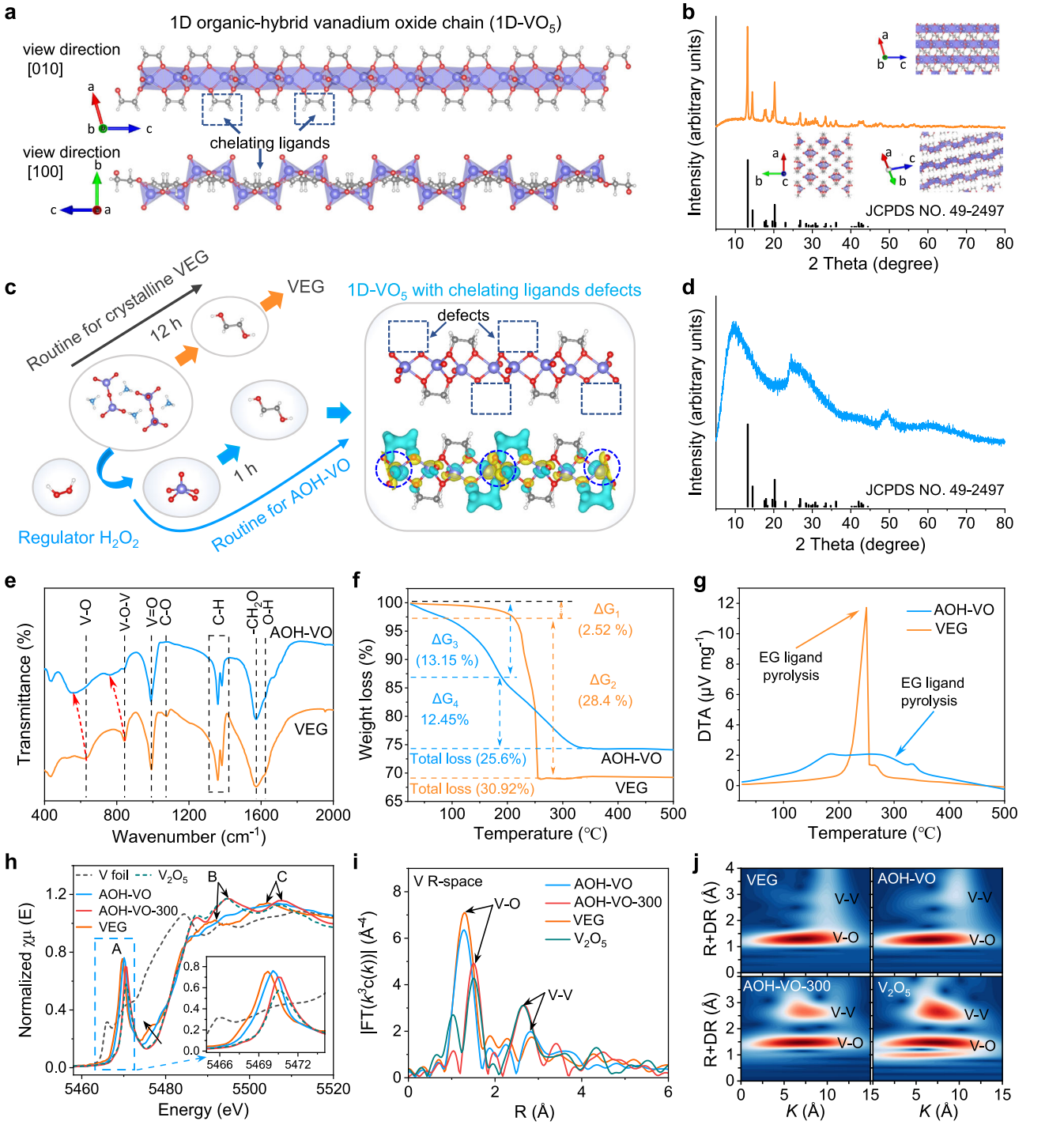

Fig. 1 | Transformation from VEG to AOH-VO. a 1D model of organic-hybrid VO_5 chains in VEG. **b** XRD pattern and 3D model of crystalline VEG. **c** Schematic illustrations for the synthesis strategy of AOH-VO. **d** XRD pattern of AOH-VO with reference Bragg peaks of VEG (black). **e** FT-IR spectra for the AOH-VO (blue) and VEG (orange). Note that the arrows in **e** indicate the significant redshift for the V-O and V-O-V bonds of AOH-VO. **f** TG, and **g** DTA curves of AOH-VO (blue) and VEG (orange) measured in an air atmosphere at a 5 °C min^{-1} heating rate. ΔG_1 and ΔG_3 are from removal of adsorbed water; ΔG_2 and ΔG_4 are from removal of chelating ligands (EG-CL). **h** V K-edge XANES spectra, **i** EXAFS spectra and **j** Wavelet transform (WT) contour plots of VEG, AOH-VO, AOH-VO-300 and standard V_2O_5.

hybrids, exhibit similar peak profiles, distinct from amorphous AOH-VO-300 and crystalline V_2O_5. Their peak positions are smaller than those of AOH-VO-300 and V_2O_5 due to structural differences. VEG and AOH-VO possess 1D edge-sharing VO_5 chains with EG-CL enlarging chain-chain distances, whereas V_2O_5 has densely packed VO_5 units in a layer-like structure. The enhanced scattering effect of the shorter V=O bond reduces the average V-O scattering distance in the 1D-VO_5 chains, differentiating the hybrids from the oxides. Meanwhile, VEG and AOH-VO exhibit higher V-O peak intensities but lower V-V peak intensities, consistent with fewer V-V interactions in their 1D-VO_5 chains structure. The higher V valence state in AOH-VO-300 and V_2O_5 might also reduce photoelectron scattering, then provide higher V-V interactions and enhanced V-V peak intensities. All these investigations indicate that the amorphous and organic-hybrid nature strongly modulate the atomic local structure making it obviously different from VEG and AOH-VO-300.

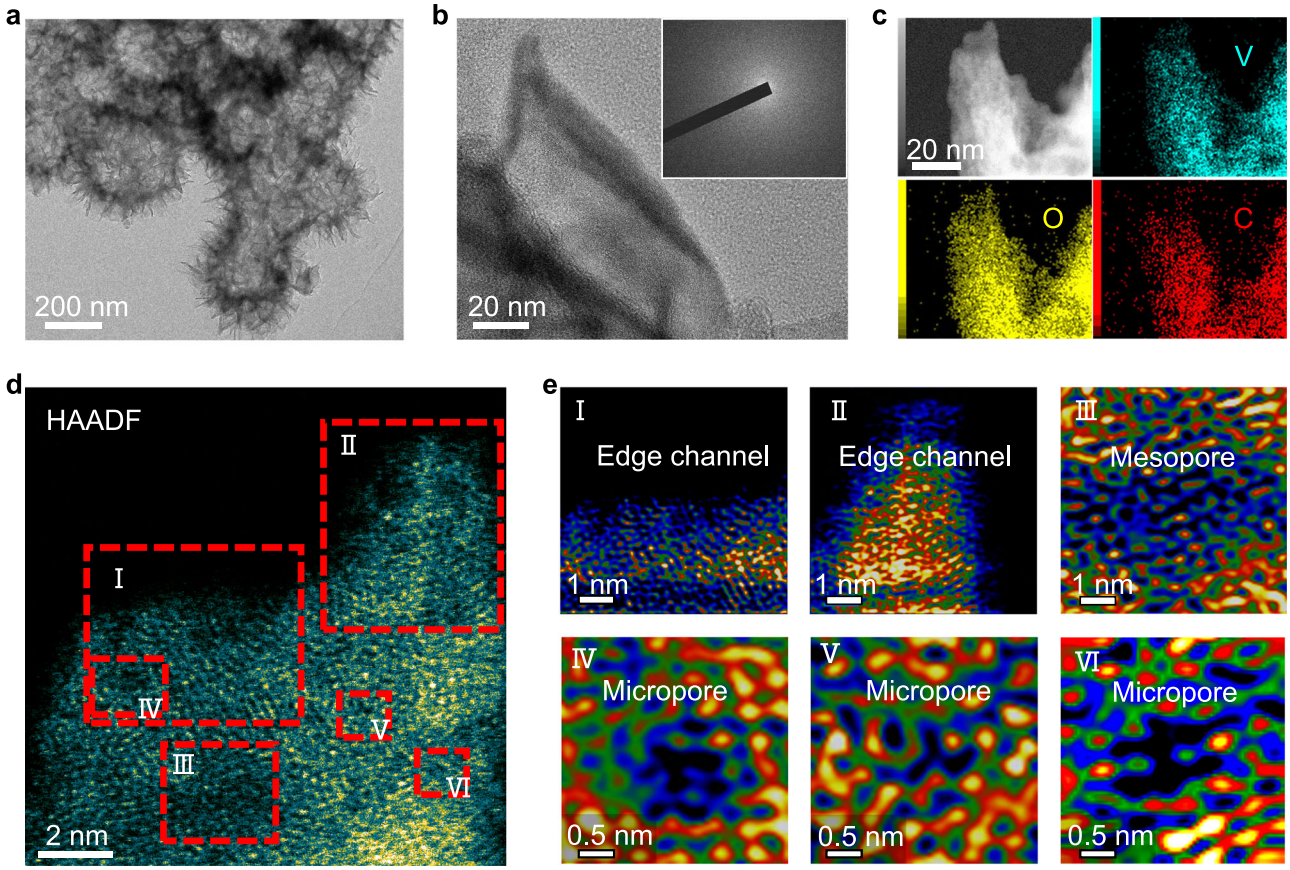

Fig. 2 | Direct observation of the microstructure of AOH-VO. a TEM image. **b** HRTEM and SAED images. **c** The elemental mappings of C, O, and V in HAADF-STEM mode. **d** Atomic-resolution HAADF-STEM image, and **e** The corresponding filtered images of the red rectangular area.

Multi-scale hierarchical structure for reversible redox reactions

Scanning electron microscope (SEM) and transmission electron microscopy (TEM) images (Supplementary Fig. 11a and Fig. 2a) reveal that the random arrangement of 1D-D-VO_5 chains in AOH-VO leads to the formation of spherical structures with hollow core diameters of approximately 200 nm and near-spherical shells of hierarchical ultrathin nanosheets, likely due to the generation of tiny bubbles during the solvothermal reaction. Elemental mapping images demonstrate a uniform distribution of V, O, and C in these hollow spherical structures (Supplementary Fig. 11b). The uniform distribution of C elements further confirms the presence of organic components, supporting FT-IR characterizations. Figure 2b shows a high-resolution transmission electron microscopy (HRTEM) image of AOH-VO, revealing that the ultrathin nanosheets exhibit a twisted lamellar structure but lack clear lattice fringes. The inset in Fig. 2b presents a selected area electron diffraction (SAED) image, which does not display distinct diffraction spots and rings, further confirming the amorphous nature of AOH-VO, consistent with the XRD and DTA results. Furthermore, the comparative SEM and TEM studies on VEG and AOH-VO-300 also evidence that AOH-VO has different crystalline structure from VEG and different organic compositions with AOH-VO-300 (Supplementary Figs. 12 and 13).

High-angle annular dark-field (HAADF) scanning transmission electron microscopy (HAADF-STEM) was used to study the atomic local structure of AOH-VO. The HAADF-STEM and elemental mapping images (Fig. 2c) present a uniform distribution of V, O, and C in the mesoporous nanosheet, evidencing the V-O unites and EG-CL-related groups distributed uniformly at the near-atomic and nanoscale. Figure 2d indicates that the V atoms in the lamellae form a chaotic disordered structure consisting of the XRD, HRTEM, and SAED observations. The random stacking of the 1D-D-VO_5 chains also resulted in many micropores in the scale of 1 ~ 2 nm. The filtered HAADF-STEM images in the region I-VI of Fig. 2d, presented with higher magnifications in Fig. 2e, provide further insights into the random structure. There are numerous edge channels on the surface of the nanosheets, and micropores near or below 1 nm can also be observed in the enlarged filtered HAADF-STEM images in regions I and II. In addition, the presence of many micropores and mesoporous channels on the surface of the AOH-VO nanosheets is evident in regions III to VI. The amorphous structure induced by the fast random packaging weakens the chain-chain interactions of 1D-D-VO_5 and creates many atomic/molecule-scale pores, facilitating electrolyte interpenetration, ion diffusion, and exposure of reaction sites, thereby possibly enhancing energy storage capabilities. The unique multiscale porous structure, spanning from near-molecule-scale gaps between the 1D-VO_5 chains, to micro-mesopores on the nanosheets, and hollow spherical structures formed by stacked nanosheets, are further confirmed by the N_2 adsorption-desorption isotherms analysis (Supplementary Fig. 14).

The galvanostatic charge-discharge (GCD) profiles of AOH-VO deliver a specific capacity of 520 mAh g^{-1} under 0.1 A g^{-1} (Supplementary Fig. 15a). The value is among the highest reports of cathode materials for AZIBs[22]. It can reach about ~88.4% of the theoretical capacity of V_2O_5 (589 mAh g^{-1}) and is much higher than the theoretical capacity of VEG (422 mAh g^{-1}), suggesting the defect of EG-CL is facilitated for improving the specific capacity due to the non-electrochemical reactivity of EG-CL. For comparison, we calculated the theoretical capacity of AOH-VO as 516 mAh g^{-1} based on TG analysis (Supplementary Note 3). Although the contents of EG-CL in the calculation might have some error (less than 10%), the experimental capacity of AOH-VO is believed to be ~100% close to or exceed (when

additional capacity from the surface capacitance is considered) the theoretical value (508 to 523 mAh g^{-1}) (Supplementary Fig. 15b). However, the specific capacities of VEG and AOH-VO-300 are far below their theoretical value, proving the unique amorphous organic-inorganic structure is the key to complete utilize the reaction sites of AOH-VO (Supplementary Fig. 15c). Cyclic voltammetry (CV) profiles of AOH-VO at 0.2 mV s^{-1} (Supplementary Fig. 16) show four redox peaks between 0.2 and 1.7 V vs. Zn/Zn^{2+}. These peaks correspond to the continuous redox couples of V^{5+}/V^{4+} and V^{4+}/V^{3+}, respectively, with no new peaks from organics-related redox process. The CV curves over 50 cycles exhibit excellent repeatability and nearly 100% capacity retention. The four redox peaks show minimal peak shifts, less than 50 mV after 50 cycles, confirming the high reversibility of the redox reactions and the stability of the reaction sites during cycling.

The reversible Zn^{2+} intercalation/deintercalation could also be confirmed by the XPS and elemental mapping analysis. The V 2*p* XPS peaks shift from high binding energy V^{4+}/V^{5+} (47%/53%) to lower binding energy V^{3+}/V^{4+} (65.9%/34.1%) with continuous Zn^{2+} intercalation (Supplementary Fig. 17a–c), indicating typical charge transfer reactions during discharge. The reduction state of V valence state after discharge could also be evidenced by the large lower energies shifts of $V\text{-}L_2$ and $V\text{-}L_3$ edges (~1.5 eV) in the electron energy loss spectroscopy (EELS) spectra (Supplementary Fig. 18). The fully discharged AOH-VO presents a homogeneously dispersed Zn element at both nano and near-atomic scales while maintaining an amorphous structure, as confirmed by elemental mapping and HAADF-STEM imaging (Supplementary Fig. 19a, b, d). Upon charge, the Zn signals in XPS spectra and elemental mapping image nearly disappear, indicating the Zn^{2+} extraction from AOH-VO (Supplementary Fig. 19c). Meanwhile, V 2*p* XPS peaks return to V^{4+}/V^{5+} (31.9%/68.1%) states (Supplementary Fig. 17c). Notably, the C 1*s* peak positions from C-O bonds remain unchanged during the charge-discharge process, suggesting that the organic ligands do not participate in the electrochemical reaction (Supplementary Fig. 17e). Ex-situ Raman and in-situ attenuated total reflectance (ATR) FT-IR analyses reveal the Zn^{2+} intercalation/deintercalation accompanied by the highly reversible red shits of V=O bonds related vibrations (Supplementary Fig. 20), suggesting the local environments of the V=O reaction sites undergo highly reversible variation in the consecutive charge-discharge processes.

The structure stability was studied by in-situ XRD measurements under four consecutive charge-discharge processes. The broad peaks in the 10° to 40° range were nearly unchanged and the 192 curves show excellent coincidence in the XRD plots (Supplementary Fig. 21a), suggesting that the amorphous structure would not transform into other crystalline phases. The near-coincident profiles suggested no volumetric expansion, which is different from crystalline active materials[13,23,24]. However, some new but weak peaks at 6.6°, 13.2°, 19.8°, and 33.2° appeared repeatedly when discharged from 0.8 to 0.2 V (Supplementary Fig. 21b). These peaks consist of the by-products formed using zinc trifluoromethanesulfonate ($Zn(OTF)_2$) aqueous electrolyte, possibly originating from $Zn_x(OTf)_y(OH)_{2x-y}{\cdot}nH_2O$ precipitation, as noted in previous reports[25,26]. This is consistent with the strengthened O-H signals in O 1*s* XPS spectra (Supplementary Fig. 17d) and the surface morphology investigations of SEM and TEM images (Supplementary Figs. 22–24). The presence of by-products containing hydroxide ions indicates that H^+ ions or water might also participate in the electrochemical reaction in AOH-VO during the discharge process[27,28]. However, the primary factor contributing to the ultrahigh specific capacity of AOH-VO remains the Zn^{2+} intercalation/deintercalation process (Supplementary Note 5 and Supplementary Fig. 25).

Fast Zn^{2+} dynamics with near barrier-free diffusion

The rate-limiting kinetics of AOH-VO were studied via CV techniques under broad sweep rates of 0.1–1000 mV s^{-1} using coin-type cells (Fig. 3a and Supplementary Fig. 26). In the range of 0.1 to 1 mV s^{-1}, *b*-values calculated at every 0.05 V are higher than 0.8 in the potential window (Fig. 3a), indicating a surface-controlled dominated energy storage mechanism. The surface-controlled contribution rates are

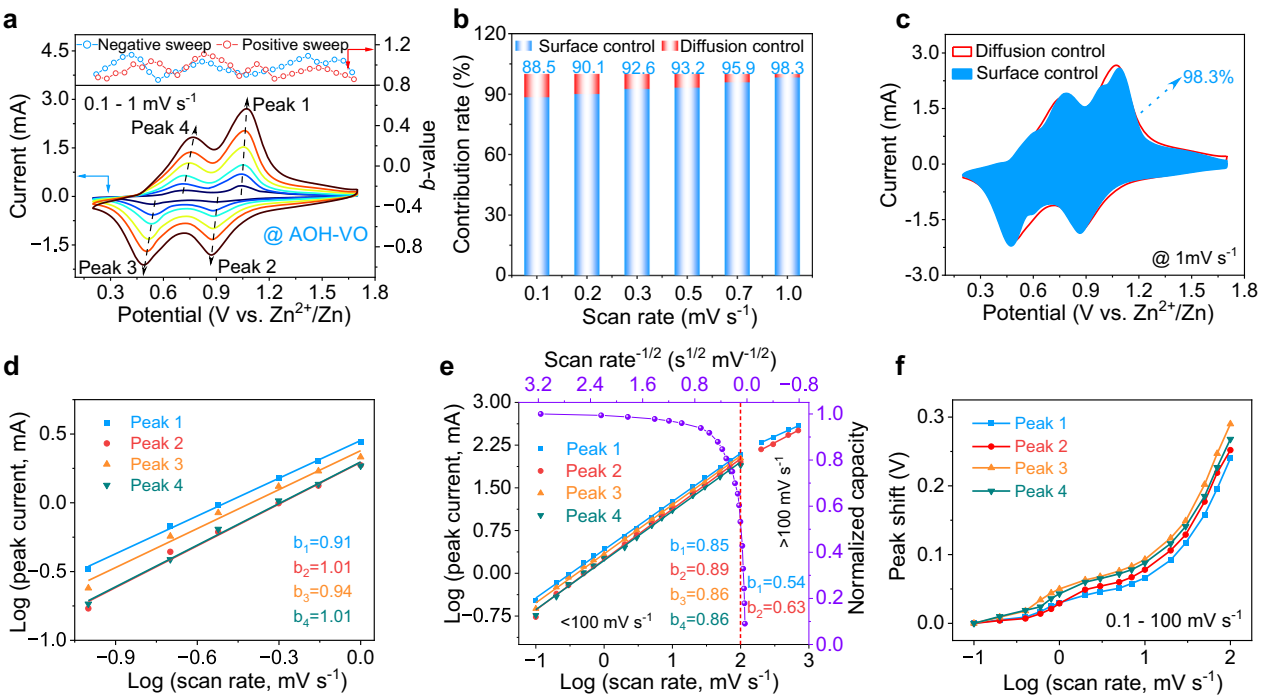

Fig. 3 | The electrochemical kinetics of the AOH-VO electrodes during the charge/discharge process. a Cyclic voltammograms (CV) curves from 0.1 to 1 mV s^{-1}. **b** The contribution ratio of the capacitive capacities and diffusion-limited capacities versus scan rate. **c** The CV profile at 1 mV s^{-1} illustrates the capacitive contribution (blue region) ratio. **d** Determination of the b-values from 0.1 to 1 mV s^{-1}. **e** The b-values from 0.1 to 1000 mV s^{-1}, along with the normalized capacity versus $v^{-1/2}$. **f** Curves of log (*v*) versus redox peaks potential shifts.

increased from 88.5% to 98.3% as scan rates rise from 0.1 to 1 mV s^{-1} (Fig. 3b, c), a significant advantage compared to the current AZIBs cathode materials. In addition, AOH-VO has larger surface-controlled contribution rates and larger b-values than VEG and AOH-VO-300 (Fig. 3d and Supplementary Figs. 27 and 28). Notably, VEG, with significantly smaller specific surface area, presents relatively higher surface control contributions than that of AOH-VO-300, suggesting that the organic ligands could markedly enhance Zn^{2+} diffusion in organic-inorganic hybrid solids.

For larger scan rates range, the logarithm profiles of scan rates and peak currents reveal a shift from surface to diffusion control below and above 100 mV s^{-1} (Fig. 3e), contrary to the conventional battery energy storage mechanism. This confusion is caused by the increased ohmic contribution or the restricted rapid diffusion of zinc ions[29,30]. The critical value in the AOH-VO of ~100 mV s^{-1} is much larger than the previously reported results. For example, among the currently reported high-power intercalation cathode materials, the transition scan rate from the surface to diffusion control process is 10–20 mV s^{-1} for pure hydrated vanadium dioxide nanoribbon (HVO)[31], VO_2(B)[32], V_2O_5@CNTs-50% composite[33]. The transient watershed of the scan rate is enhanced to 50 mV s^{-1} in the interface-dominated storage of VO_x-G heterostructures[29]. Compared with these materials, AOH-VO has remarkably fast kinetic properties, possibly from its multi-scale hierarchical structures composed of randomly packed polymer-like 1D chains. Furthermore, the peak shifts of AOH-VO for peaks 1–4 are all less than 300 mV as the scan rates increase from 0.1 to 100 mV s^{-1} (Fig. 3f). In contrast, VEG and AOH-VO-300 endure peak shifts of 150–300 mV and 50–120 mV, respectively, even in a much smaller scan rate range from 0.1 to 3 mV s^{-1}. It is noted that VEG endurances much larger electrochemical polarization, suggesting the amorphous induced large ion diffusion channels also contribute to the rapid electrochemical kinetics of AOH-VO.

The activation energy determines the ion diffusion kinetics from the electrolyte to the interface and solid materials. Usually, the activation energy for the ion diffusion in the electrolyte is the smallest among these three processes. At room temperature, 3 M $Zn(OTF)_2$ aqueous solution exhibits a conductivity of 47.4 mS cm^{-1}, closely aligning with previously reported values[34] (Fig. 4a, Supplementary Fig. 29a and Supplementary Table 5). This conductivity is about three-order magnitude higher than the trifluoromethanesulfonic acid aqueous solution with the same pH value (Supplementary Fig. 25h), indicating the major carriers are from $Zn(OTF)_2$. The activation energies of conduction (E_{ac}) in $Zn(OTF)_2$ were increased from 10.9 to 18.2 kJ mol^{-1} as the concentration rose from 1 to 4 M. Specifically, the E_{ac} of 3 M $Zn(OTF)_2$ was determined to be 17.9 kJ mol^{-1} (Supplementary Fig. 29b). The diffusion coefficient of the electrolyte was estimated to be 10^{-6} cm^2 S^{-1} (Supplementary Fig. 29c and Supplementary Note 6), meanwhile the activation energy for the ion diffusion in the electrolyte (E_{ad}) was calculated as 13.2 kJ mol^{-1} (Fig. 4a, Supplementary Fig. 29d and Supplementary Table 5). The similar values of the E_{ac} and E_{ad} suggested that the small external electric field does not affect the interaction and chemical environment significantly during the ion diffusion and transportation in the electrolyte.

Typically, the charge transfer from the electrolyte into the solid framework requires overcoming a substantial activation energy barrier (E_{act}). The analysis on temperature-dependent electrochemical impedance spectra (EIS) of the AOH-VO, VEG, and AOH-VO-300 cathodes (Supplementary Fig. 30a–d), revealed that AOH-VO has the lowest charge transfer resistance (R_{ct}) of 10.14 Ω compared to 238.5 and 203 Ω of VEG and AOH-VO-300 cathode at 20 °C (Supplementary Fig. 30e). The calculated E_{act} values for AOH-VO, VEG, and AOH-VO-300 are 6.3, 25.2, and 16.7 kJ mol^{-1}, respectively (Supplementary Fig. 30f–i). The low E_{act} of AOH-VO corresponds well with its ultra-small R_{ct} value compared to VEG and AOH-VO-300. We note that the E_{act} is even smaller than the E_{ad}, suggesting that the Zn^{2+} could nearly freely diffuse from the electrolyte into AOH-VO. This fast interfacial dynamic was rarely reported in fast-charging batteries[28,35].

When it comes to the Zn^{2+} diffusion in the solid framework, the room temperature galvanostatic intermittent titration technique (GITT) investigation shows that the D_{Zn} value of Zn/AOH-VO batteries are as high as 10^{-8} to 10^{-9} cm^2 s^{-1}, much larger than in VEG and AOH-VO-300, and also higher than most of the reported aqueous ZIBs cathode materials (Fig. 4b, Supplementary Table 6 and Supplementary Note 7). Notably, the high D_{s0} (10^{-8} cm^2 S^{-1}) in the AOH-VO significantly reduces the difference between the D_{s0} in the solid and the D_{e0} in the electrolyte from 5 to 2 orders of magnitude. The high diffusion coefficient contributes considerably to the fast dynamic process during the reversible Zn^{2+} (de)intercalation.

The activation energy for Zn^{2+} diffusion in the solid framework (E_{asf}) was further evaluated by the temperature-dependent GITT from 25, 40, and 55 °C (Supplementary Fig. 31a), which is theoretically feasible but not yet reported in the literature. Figure 4c shows the ion diffusion coefficients during the four consecutive charge-discharge processes with excellent repeatability. All the D_{Zn} values are located in the range of 10^{-8}–10^{-9} cm^2 s^{-1}, increasing slightly with the operating temperatures. Figure 4d and Supplementary Fig. 31c show that the AOH-VO has an ultralow ion diffusion activation energy of 7.8 kJ mol^{-1} in the initial state. It becomes higher as the depth of the discharge process increases, while the opposite behavior could be observed during the reversible charging process. This phenomenon might be due to the repulsive forces between the intercalated Zn^{2+} ions, making it harder to find suitable sites during the sustained intercalation discharge process. Nonetheless, the maximum E_{asf} (20.3 kJ mol^{-1}) for AOH-VO is still closer to the E_{ac}, suggesting that the Zn^{2+} ions could near-freely diffuse into the solid active materials even under the strong Zn^{2+} repulsions.

The DFT method was used to understand the effect of 1D-VO_5 chains interaction on the energy barriers of Zn^{2+} diffusion (Supplementary Fig. 32a–c). The E_b of Zn^{2+} diffusion in the 3D VEG lattice is 1.16 and 2.23 eV along the a-axis and c-axis pathways, respectively. For the 1D-VO_5 model simulating randomly stacked 1D units without strong chain-chain interaction, we only compared the E_b in the c-axis direction between the 3D and 1D models. The E_b for 1D-VO_5 is significantly smaller at 0.51 eV, compared to the 3D simulation result (2.23 eV), indicating that reducing chain-chain interaction could substantially lower the Zn^{2+} interaction with the skeleton and accelerate ion diffusion kinetics. In the presence of EG-CL defects, the E_b of Zn^{2+} diffusion along the c-axis pathway in the 3D-D-VEG decreased, but it increased along the a-axis pathway (Supplementary Fig. 32d, e). However, the E_b for the 1D-D-VO_5 is only slightly smaller than 1D-VO_5 (~0.01 eV decrease) (Supplementary Fig. 32f) and also significantly smaller than the 3D-D-VEG and 3D-VEG. This comparative analysis confirmed that the weak 1D-D-VO_5 chain-chain interactions of AOH-VO due to amorphous effect play a key role in decreasing E_b of Zn^{2+} diffusion compared with the EG-CL defect (Supplementary Fig. 32g).

We also tried to determine the E_{asf} of VEG and AOH-VO-300 (Supplementary Fig. 33). The E_{asf} ranged from 31.2 to 138.4 kJ/mol for VEG, but reliable data were not obtained for AOH-VO-300 due to its poor stability. We found that the maximum value of E_{asf} for AOH-VO is also smaller than the minimum value of E_{asf} for VEG (i.e. at initial state, ~31.2 kJ mol^{-1}) during charge-discharge, which provides strong evidence for the priority of the amorphous strategy on the organic-hybrid crystalline materials. The E_{asf} of AOH-VO and VEG correspond to average energy barriers of 0.08–0.21 eV and 0.32–1.43 eV. The experimental results are all smaller than the E_b calculated by the DFT method because they are average values for all the diffusion paths. We have to note that the simulated energy barrier of the 1D structure is nearly the highest energy if the 3D diffusion effect is considered. The vertical diffusion for the 1D structure is nearly free, and the theoretical E_{asf} should be in the range of 0–0.50 eV, which is a reasonable

https://doi.org/10.1038/s41467-024-55000-8

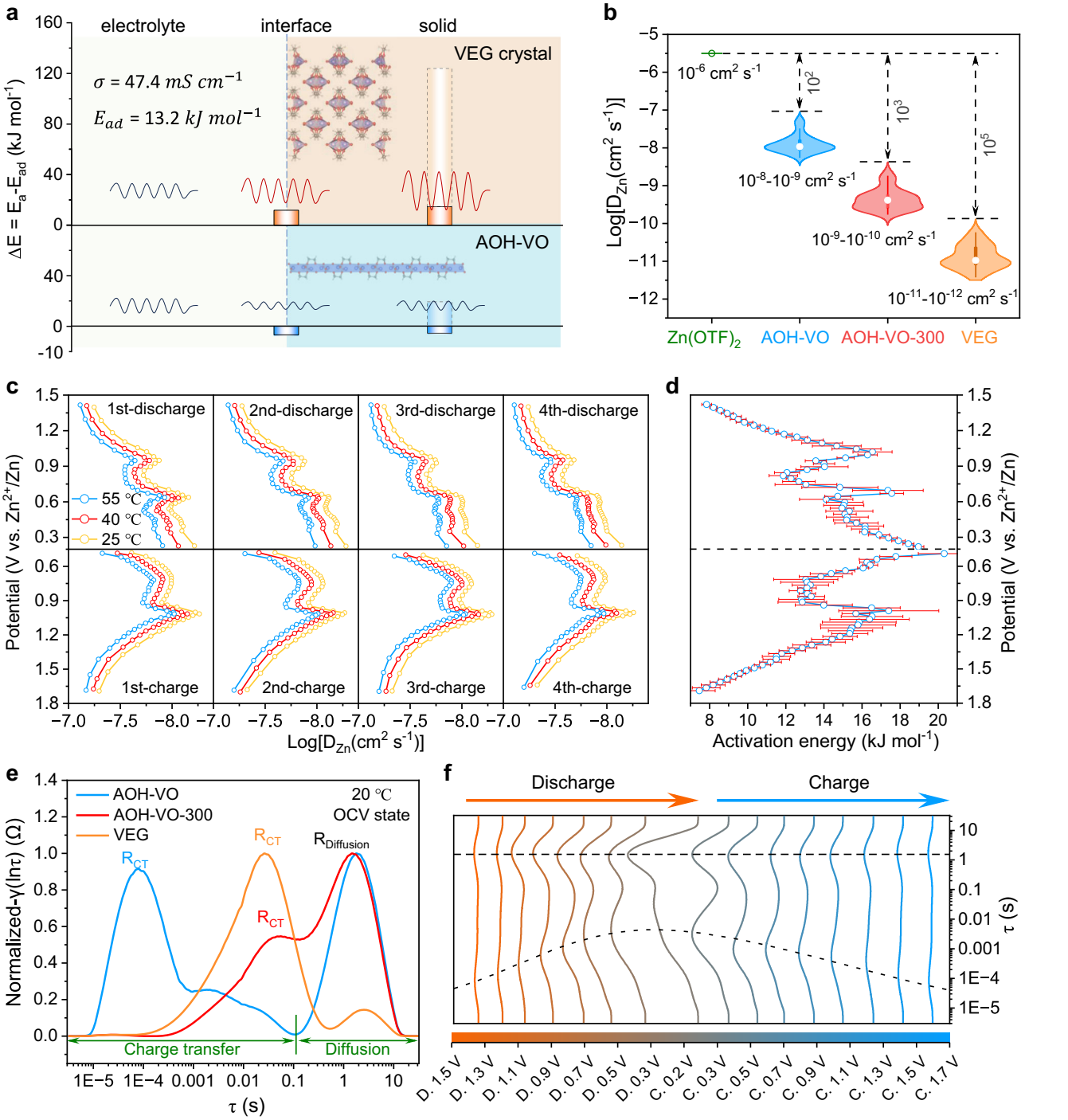

Fig. 4 | Near barrier-free Zn^{2+} dynamics of AOH-VO in AZIBs. a Schematic diagram of activation energies for Zn^{2+} diffusion in the electrolyte, across the interface, and in the solids. **b** Zn^{2+} diffusion coefficients in the electrolyte and the solids of AOH-VO, AOH-VO-300, and VEG. **c** Temperature-dependent Zn^{2+} diffusion kinetics for four consecutive cycles of AOH-VO. **d** The evolution of activation energy for Zn^{2+} diffusion in AOH-VO during the charge-discharge process. Error bars indicate the standard deviation of the four cycles experiments. **e** DRT plots of AOH-VO, AOH-VO-300, and VEG under the open circuit potential at 20 °C. **f** The DRT plots of AOH-VO during reversible Zn^{2+} insertion/extraction processes.

coincidence with the experimental results. The near-free ion diffusion channels in these randomly packed 1D-D-VO_5 networks could significantly reduce the E_{asf} of Zn^{2+} diffusion, thereby significantly promoting the rate capabilities.

Figure 4e shows the distribution of relaxation time (DRT) profiles with normalized vertical coordinates for AOH-VO, VEG, and AOH-VO-300. The near symmetrical peaks with relaxation time (τ) in the range of 0.1–32 s correspond to the electrolyte diffusion-polarization response under AC signals in the open-circuit state. The peaks with τ < 0.1 s correspond to the complex charge transfer processes. AOH-VO has a strong ultrafast response peak centered at 8.15×10^{-5} s, about three orders faster than the dominant response time of AOH-VO-300 and VEG, suggesting that the unique structure of AOH-VO could provide ultrafast reaction pathways. AOH-VO also has two weak response

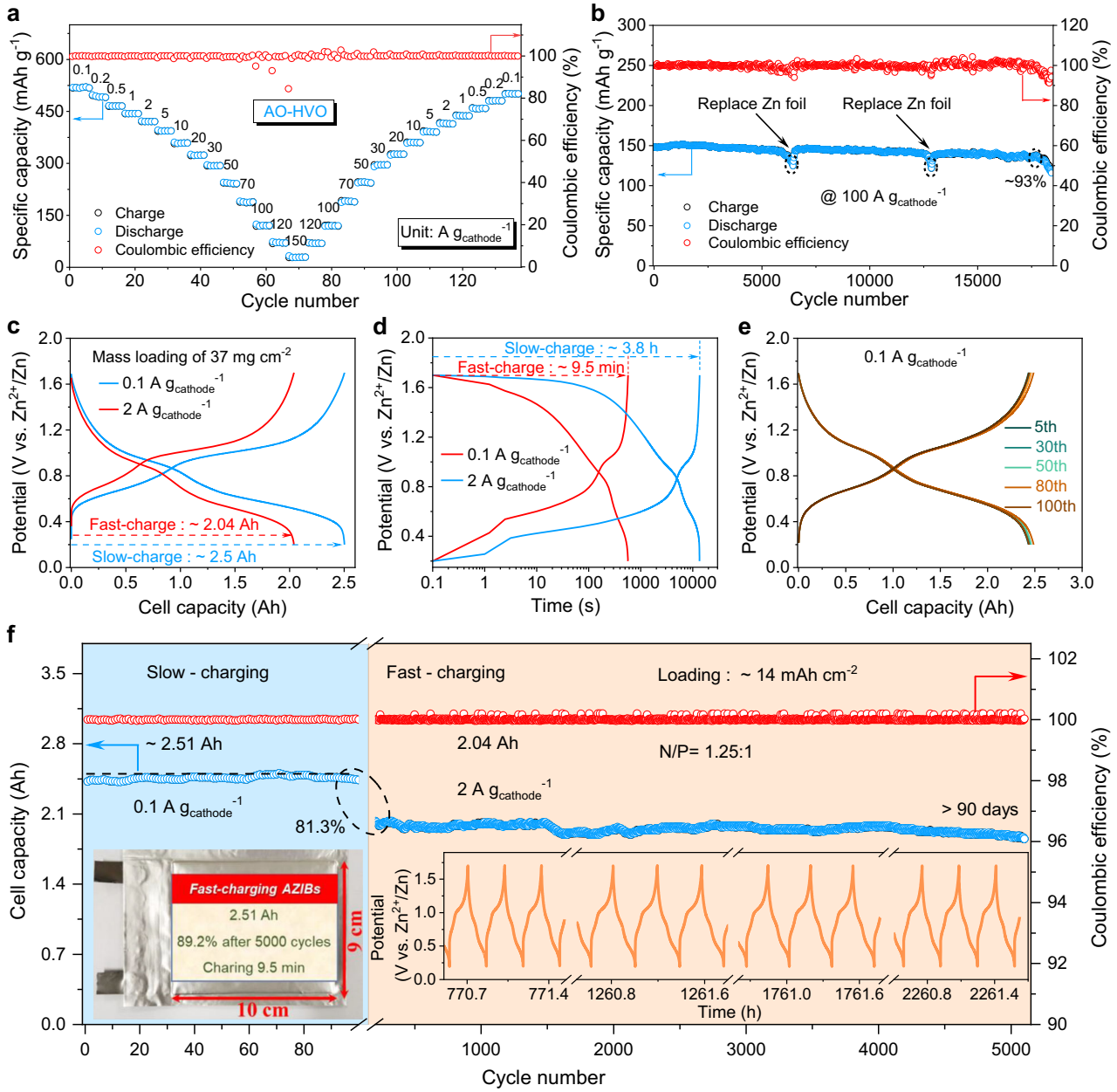

Fig. 5 | Electrochemical performance of AOH-VO cathodes assembled coin cells and Ah-level fast-charging double-layer pouch cell. a Rate capability based on the mass of AOH-VO cathode materials (Active material loading mass: 1.5 mg cm^{-2}, electrolyte amount: 100 μL) for coin cell at different specific currents and **b** Long-cycle stability performance at a high specific current of 100 A g^{-1}. **c** Ah-level capacity based on the mass of AOH-VO cathode materials (Active material loading mass: 37 mg cm^{-2}, electrolyte amount: 12 mL) for fast-charging pouch cell at 0.1 A g^{-1} (slow-charge) and 2 A g^{-1} (fast-charge). **d** Typical charging time by Ah-level pouch cells during fast and slow charge-discharge. **e** Galvanostatic charge-discharge profiles of the 2.5 Ah pouch cell at selected cycles at 0.1 A g^{-1}. **f** The capacity and coulombic efficiency of the pouch cells during long cycling from 0.1 A g^{-1} to 2 A g^{-1}. The insets show the pouch cell photograph and the representative voltage profiles.

peaks at 0.002 to 0.038 s, much close to AOH-VO-300 and VEG. They are probably due to some dense stacking parts, as observed in the TEM images.

The DRT curves obtained from in-situ EIS spectra of AOH-VO during the charge-discharge process are presented in Supplementary Fig. 35 and Fig. 4f. The relaxation time in the high-frequency region is prolonged as the discharge process proceeds, suggesting that continued surface adsorption of Zn^{2+} and framework intercalation leads to a retardation of the kinetics. Conversely, the continued extraction/desorption of Zn^{2+} during charging accelerates the Zn^{2+} dynamic process. Furthermore, the dominant relaxation time of AOH-VO at the discharge state is still much shorter than the initial relaxation time of AOH-VO-300 and VEG. These observations are consistent well with the evolution of E_{asf}, confirming that the activation energy in the solid framework controls the Zn dynamic process.

Stable fast-charging performance

The near barrier-free diffusion from the electrolyte to the solid framework enables ultrafast Zn^{2+} dynamics for exceptional superior rate performance of the AOH-VO as demonstrated in Fig. 5a and Supplementary Fig. 36. It could maintain 85.3%, 80.8%, 75.7%, 69% and 56.4% of initial capacity (0.1 A g^{-1}) at 1, 2, 5, 10 and 30 A g^{-1}. Surprisingly, it can deliver a capacity of 121 mAh g^{-1} at an ultrahigh specific current of 100 A g^{-1}, taking only 4.3 s to discharge fully. A slight decline of the

platform voltage is still visible, revealing redox reactions at 100 A g^{-1} (Supplementary Fig. 36). This rate capability signifies a capacity retention of 23.2% for a 1000-fold increase from 0.1 to 100 A g^{-1}. To the best of our knowledge, this is one of the highest rate capabilities among the reported cathode materials without any highly conductive active carbon supports such as graphene, carbon nanotube, and carbon nanofiber (Supplementary Table 6). Furthermore, the reversible capacity can maintain 29 mAh g^{-1} even at 150 A g^{-1} and the specific discharge capacity can still return to 512 mAh g^{-1} when back to 0.1 A g^{-1}, comparable with its initial specific discharge capacity. In addition, a significant study suggests that H^+ insertion becomes more predominant as the rates increase[27,36]. The comparison of asymmetric and symmetric cells indicates that H^+ ions, due to their low concentration and conductivity in the electrolyte, cannot effectively participate in high-rate redox reactions (Supplementary Fig. 37 and Supplementary Note 5). This is further supported by the decreased by-product XRD peak observed in the discharged AOH-VO at high specific currents (Supplementary Fig. 38).

AOH-VO also presents excellent electrochemical stability with the capacity retention maintaining 98%, 92.4%, 92.9% after cycling at 0.2 A g^{-1} with 200 cycles, 1 A g^{-1} with 800 cycles, and 10 A g^{-1} with 11,281 cycles, respectively (Supplementary Fig. 39). It can even endure over 25,000 cycles with better than 90% capacity retention at 30 A g^{-1} (Supplementary Fig. 40a). The SEM images (Supplementary Fig. 40b) and FT-IR patterns (Supplementary Fig. 40c) after the 5,000th to 27,325th cycles shows that their surface morphologies are well-maintained with minimal structural deterioration, and the VO_5-related vibrations (V-O, V-O-V, V=O) and EG-related peaks (C-H, C−O, -CH_2O) of the AOH-VO remain stable during the high-rate long-term cycling tests. Meanwhile, SEM images and XRD patterns of the Zn anode show no dendrites after the 5,000th to 25,000th cycles (Supplementary Fig. 41), crucial for excellent long-term cycling stability. However, significant zinc anode corrosion and the appearance of by-product XRD peaks occur by the 27,325th cycle, leading to battery failure.

Additionally, AOH-VO was tested at an ultrahigh rate of 100 A g^{-1} using a separable cell. Figure 5b shows that AOH-VO retains 98% of its capacity after 5,000 cycles, with only a 0.4% decay per 1,000 cycles. To mitigate capacity decay due to zinc anode corrosion, the Zn foil anode and electrolytes were replaced after 6,441, 12,861, and 18,421 cycles. Stable cycling beyond 17,000 cycles at 100 A g^{-1} was observed with periodic replacement of the Zn foil anode, maintaining over 93% capacity retention. These experiments demonstrate the structural stability of the AOH-VO electrode material even at ultrahigh rates. In contrast, SEM images and XRD patterns of the zinc anode after 6,441, 12,861, and 18,421 cycles at 100 A g^{-1} (Supplementary Fig. 42) reveal severe dendrite formation and strong by-product XRD patterns. These observations suggest that cell failure is likely due to hydrogen evolution and dendrite formation during ultrafast charge-discharge cycling, rather than degradation of the AOH-VO cathode material.

In comparison to AOH-VO, VEG, and AOH-VO-300 display significantly lower rate retentions and cycling retentions at the same specific current (Supplementary Figs. 43 and 44). Both AOH-VO and VEG feature edge-sharing VO_5 chains, which are theoretically more stable than point-sharing structures (Supplementary Fig. 45). The EG-CL provides additional protection to these edge-sharing chains, preventing water molecules from causing dissolution. Consequently, AOH-VO and VEG demonstrate excellent chemical stability with minimal ion leaching—approximately one percent of that of AOH-VO-300 after 15 days (Supplementary Fig. 46). EG-CL also prevents the formation of a densely packed V-O-V-O amorphous network, creating larger and more stable ion diffusion channels compared to AOH-VO-300, and fully exposing reaction sites for redox reactions compared to VEG. The cycling stabilities of VEG and AOH-VO-300 show that chemical stability dominates cycling retention at low specific currents, while electrochemical-induced structural deterioration strongly affects high-rate cycling retention. Thus, the combination of a chemically stable atomic structure and large ion diffusion channels collectively contributes to the overall cycling stability performance. Digital images of the glass fiber separators of Zn/AOH-VO, Zn/AOH-VO-300, and Zn/VEG batteries after cycling (Supplementary Fig. 47) further confirm that the unique structure of AOH-VO could inhibit both the chemical and electrochemical dissolution during cycling.

The AOH-VO cathode outperforms most reported vanadium-based cathodes for AZIBs in specific capacity, rate performance, and long-term cycling stability across a wide range of specific currents, and demonstrates superior electrochemical performance compared to both crystalline and amorphous vanadium-based oxides, with or without conductive substrates (Supplementary Fig. 48a, b and Table 6). The Ragone plot of AOH-VO cathode (Supplementary Fig. 48c) present a remarkable energy density of 426.9 Wh kg^{-1} at a power density of 82 W kg^{-1} (based on the mass of AOH-VO, Supplementary Note 9), and an ultrahigh power density of 77217.4 W kg^{-1} at an energy density of 14.8 Wh kg^{-1}. The highest energy density and highest power density that could be achieved are much superior to most Zn-ion batteries based on the cathodes of various popular cathode materials[25,37–45]. Significantly, AOH-VO has an ultra-high power density of 71581.4 W kg^{-1} at 100 A g^{-1} and maintains a high energy density of 85.5 Wh kg^{-1}, which is even superior to the nitrogen-doped graphene in high-power supercapacitors (Maximum power density: 44000 W kg^{-1} and maximum energy density: 63 Wh kg^{-1})[46]. Therefore, besides electric vehicles, this fast-charging Zn/AOH-VO battery might also have extraordinary significance for a wide range of applications in large intermittent grid-scale energy storage plants, port crane lifting equipment, and traction and braking devices for transportation machinery, covering the prominent demand scenarios for high energy and power density, as well as ultra-high safety and cycling stability.

To demonstrate the potential application for ultrafast-charging batteries, the Zn/AOH-VO cell was charged at 100 A g^{-1} and discharged at different currents, as shown in Supplementary Fig. 49a, b. The charging process can be finished in 5.2 s, and the battery delivers almost the same capacity of about 149 mAh g^{-1} when discharging at specific currents in the range of 0.1 to 100 A g^{-1} (Supplementary Fig. 49c, d). High mass loading is also important for real applications. The AOH-VO electrodes with different mass loading of 1.5, 3, 6 and 10 mg cm^{-2} deliver a high capacity of 520, 517, 503 and 472 mAh g^{-1} at 0.1 A g^{-1} (Supplementary Fig. 50a, b) and a decreased capacity of 324, 252, 159 and 30 mAh g^{-1} at 20 A g^{-1} (Supplementary Fig. 50c). At a practical mass loading of 10 mg cm^{-2}, the AOH-VO still shows 4.72 mAh cm^{-2} at 1 mA cm^{-2} and 1.32 mAh cm^{-2} at 100 mA cm^{-2}, presenting to a more gradual decay in areal capacity compared to other high rate and high mass loading electrodes (Supplementary Fig. 50d, e)[29,47–50].

We further assembled a double-layer pouch cell of 9 cm × 10 cm (Supplementary Fig. 51 and inset in Fig. 5f). The pouch cell was prepared with a high mass loading of 37 mg cm^{-2} using the lamination technique. The N (30 μm, 17.37 mAh cm^{-2})/P (13.94 mAh cm^{-2}) ratio was strictly controlled at 1.25:1, and the E (3 M $Zn(OTF)_2$ electrolyte: 12 mL)/C (capacity: 2.51 Ah) ratio was 6.65 g Ah^{-1} (Supplementary Fig. 52 and Supplementary Table 7). Considering the severe corrosion of zinc anode during long term cycling, we introduced three-dimensional N-doped carbon nanofibers (NCNFs) as interlayers to prevent hydrogen evolution, dendrite formation, and reduce corrosion[51,52]. The use of NCNFs as an interlayer between the Zn anode and the separator (NCNFs-Zn) could extend cycle life (750 cycles with high Coulombic efficiency vs. 200 cycles for Zn/Ti cells), and demonstrate superior stability (1968 hours) and rapid desolvation capabilities (27.6 kJ mol^{-1} vs. 40.7 kJ mol^{-1} for bare Zn) (Supplementary Figs. 53–55).

The pouch cell has an initial capacity of 2.42 Ah at 0.1 A g^{-1}, and achieves a maximum capacity of 2.51 Ah (376 mAh g^{-1} based on the mass of AOH-VO) up to the 71st cycle, with a corresponding charging

time of 3.8 h (Fig. 5c, f). When worked at a specific current of 2 A g^{-1}, a high-rate performance of 2.04 Ah (306 mAh g^{-1}) could be reached, i.e., 81.3% of the maximum charging capacity at 0.1 A g^{-1} could be maintained. The fast-charging time is only 9.5 min less than 15 min (Fig. 5d). These results suggested that the fast-charging performance of the pouch cell with large area and high mass load could meet the U.S. Department of Energy requirements for the practical application of XFC devices. The pouch cell was cycled at a low specific current of 0.1 A g^{-1} (one cycle of about 7.6 h) for 101 cycles, and the capacity was retained at almost the same rate as the initial value (Fig. 5e). As the specific current is increased to 2 A g^{-1}, the pouch cell achieves 90.7% capacity retention after 5000 cycles (Fig. 5f), and no noticeable swelling is observed even after the cycling test (Supplementary Fig. 55e, f). Under such harsh conditions, the pouch cell stably sustained for >90 days (3.1 months) with the average coulombic efficiency higher than ~99.9%. These demonstrations indicate that AOH-VO is a promising and ideal candidate for the development of practical ultrafast-charging AZIBs.

In summary, we report an amorphous organic-hybrid vanadium oxide (AOH-VO) with abundant atomic/molecular-level pores formed by randomly assembling 1D-D-VO_5 chains with weak interactions, which can fully expose the active sites to the electrolyte. Most importantly, it can also significantly reduce the E_a for Zn^{2+} diffusion from the electrolyte into the solids, about 6.3 kJ mol^{-1} for the interface process and 7.8 kJ mol^{-1} for the internal migration in solid. These values are notably smaller than the E_a in the electrolyte (13.2 kJ mol^{-1}), indicating the near-barrier-free Zn^{2+} dynamics and enabling ultrafast charge-discharge process. Additionally, the weakened interaction between Zn^{2+} and the skeleton enhances stability, exhibiting over 17,000 cycles at 100 A g^{-1}. The assembled pouch cell presents a capacity of 2.04 Ah at 2 A g^{-1} (~81.3% of the capacity at 0.1 A g^{-1}) and could be charged in only 9.5 min and stably sustained for >5000 cycles. These results underscore the potential of AOH-VO for stable, safe, and ultrafast-charging AZIBs. Our study in this work offers innovative insights in promoting the ion dynamics for ultrafast charging metal ion batteries and opens promising avenues for developing battery materials with high capacity and ultrafast dynamics.

Methods

Materials synthesis

AOH-VO. The AOH-VO is prepared through a solvothermal method. In a typical procedure, 2 mmol ammonium metavanadate was dissolved in 15 mL of ethylene glycol with 2 mL H_2O_2 under vigorous stirring at room temperature for 2 h. Then, the mixed solution was loaded into a 25 mL autoclave with a Teflon liner and held at 200 °C for 1 h. After the reaction, the precipitate is collected and thoroughly washed with deionized water and ethanol and then dried at 60 °C for 12 h.

VEG and AOH-VO-300. To assess the regulator effect, samples 1-7 were prepared by modifying H_2O_2 quantities (Supplementary Table 1) using a procedure similar to AOH-VO, with a 12 h reaction time due to low VEG yield. Furthermore, sample AOH-VO-300 was derived from AOH-VO via calcination at 300 °C in air, employing a heating rate of 5 °C min^{-1}.

For details of materials used, see the experimental section in Supplementary Information.

Materials characterization

XRD. Powder X-ray diffraction (XRD) patterns were recorded on a Rigaku D/MAX-2500 X-ray diffractometer equipped with a Cu Kα radiation source (1.5046 Å).

For in-situ XRD measurements, AOH-VO as active material mixed with 20% acetylene black and 10% polytetrafluoroethylene binder were coated on stainless steel mesh with active material loading about 10 mg cm^{-2}. The electrode was assembled similarly to a pouch cell configuration with a cutting hole (~10 mm in diameter, sealed with polyimide film) in the cathode side of Al soft plastic film for passing through the X-ray. The cell was fully discharged/charged in four consecutive cycles at a specific current of 0.1 A g^{-1} between 0.2 V and 1.7 V using a LANHE battery electrochemical test M340A (Wuhan LAND Electronic Co. Ltd.).

FT-IR. Fourier transform infrared (FT-IR) spectra were obtained on Magna 560 FT-IR spectrometer with a resolution of 1 cm^{-1}.

For in-situ FT-IR measurements, the cell was prepared similar to that in the in-situ XRD measurement, except that the cutting hole (~20 × 20 mm^2) was sealed with a germanium substrate with a thickness of 0.7 mm for passing through the infrared ray. The cell was fully discharged/charged in two consecutive cycles at a specific current of 0.1 A g^{-1} between 0.2 V and 1.7 V using a LANHE battery electrochemical test M340A.

XAS. Each sample for the V K-edge XAS analysis was characterized as follows. V K-edge XAS (hard-XAS) measurements were conducted using an advanced synchrotron light source at the BL08B2 beamline of SPring-8 (8 GeV, 100 mA) in Japan. The X-ray beam was monochromatized with a water-cooled Si (111) double-crystal monochromator. All the V K-edge XAS spectra were measured in transmission mode, and V metal spectra were obtained as reference data at the same time to calibrate the energy.

For additional material structure characterization, see the experimental section in the supplementary information.

Electrochemical characterization

Coin cells. Detailed preparation procedures and component parameters for coin cells are described in Supplementary Note 4 and Supplementary Table 4. Zn foil (thickness: 50 um, 99.999%, Wenghe Metal) was polished with 2000 and 5000 mesh sandpaper, respectively, and used directly as anode. For coin cells, the cathodes were made by casting a mixture that contained AOH-VO powder (70 wt %), carbon black (20 wt %), and PVDF (10 wt %), onto stainless steel mesh (300 mesh, diameter: 12 mm, thickness: 0.1 mm, denoted as SS). The SS loaded with AOH-VO (AOH-VO/SS), Zn foil (diameter: 14 mm), 3 M $Zn(OTF)_2$, (100 μL) and glass fiber (Whatman, Grade GF/A, diameter: 16 mm, thickness: 200 μm, average pore diameter: 1.6 μm) were used as the cathode, anode, electrolyte and separator respectively (the mass loading of the active AOH-VO in the cathode: 1.5 mg cm^{-2}).

The detailed electrochemical characterizations on AOH-VO were performed using a LANHE battery electrochemical testers M340A (Wuhan LAND Electronic Co. Ltd.) based on CR-2032 coin-type cells with a potential window of 0.2-1.7 V (vs. Zn^{2+}/Zn). Galvanostatic charge-discharge test with a rate specific current range of 0.1-150 A g^{-1}. Long-term cycling tests were conducted using specific currents of 0.2, 1, 10, 30 and 100 A g^{-1}, respectively. All cyclic voltammetry (CV) curves were measured using an electrochemical workstation (CH Instrument 660D) with a scan rate of 0.1–1000 mV s^{-1}. The specific capacities and energy/power densities tested with coin cells were calculated based on the mass of the cathode active material. Supplementary Note 9 presents detailed calculations of specific energy/power densities. All electrochemical test experiments were performed at room temperature in an air environment.

In principle, the currents (i) of CV obey a power-law formula with the scan rates (v) according to Eq. (1):

$$i = av^b \tag{1}$$

where a and b refer to adjustable parameters. The relative contributions of the surface-controlled effect (k_1v) and diffusion processes

($k_2\upsilon^{1/2}$) could be quantitatively determined by the following equation:

$$i = k_1\upsilon + k_2\upsilon^{1/2} \quad (2)$$

where k_1 and k_2 are the corresponding constants at different sweep rates.

The temperature-dependent conductivities of zinc $Zn(OTF)_2$ aqueous solution were measured to estimate the activation energy for the Zn^{2+} conduction (E_{ac}) in the electrolyte according to the equations of (3)[53] (Supplementary Fig. 29 and Supplementary Note 6):

$$\sigma = f(T)e^{\frac{-E_{ac}}{k_BT}} \quad (3)$$

where σ is the ionic conductivity, k_B is the Boltzmann constant, T is the temperature, $f(T)$ is the pre-exponential factor, which is a constant but sometimes contains a factor $1/T$.

The concentration-dependent conductivity could also estimate the diffusion coefficient through the Nernst-Einstein equation:

$$D = \frac{RT\lambda_0}{F^2|Z|} \quad (4)$$

Where R is the gas constant (8.314 J mol^{-1} K^{-1}), T is the absolute temperature (K), F is the Faraday constant (96,493 C mol^{-1}), $|Z|$ is the absolute value of the ionic charge. λ_0 is the limiting ionic equivalent conductivity (m^2 S mol^{-1}). Then, the activation energy for the Zn^{2+} diffusion in the electrolyte (E_{ad}) could be determined via the Eq. (5):

$$D = D_{e0}e^{\frac{-E_{ad}}{k_BT}} \quad (5)$$

Where D is the ionic diffusion coefficient, D_{e0} is the pre-exponential factor in electrolyte.

Temperature-dependent electrochemical impedance spectra (EIS) of the AOH-VO, VEG, and AOH-VO-300 cathodes were measured at an open-circuit voltage (OCV) from 20 to 60 °C for comparison (Supplementary Fig. 34a–c). Charge transfer resistance (R_{ct}) were obtained by fitting the EIS spectra with ZView2 software, according to the equivalent circuit diagram in Supplementary Fig. 30d. The activation energy barrier during the charge transfer process (E_{act}) was determined by fitting the Arrhenius equation of temperature-dependent R_{ct}:

$$\frac{1}{R_{ct}} = A_0\, e^{-\frac{E_{act}}{k_BT}} \quad (6)$$

A_0 is a pre-exponential constant, R is the ideal gas constant, and T is the absolute temperature.

Electrochemical impedance spectroscopy. The electrochemical impedance spectroscopy (EIS) tests were conducted with a Solartron electrochemical station using coin cells. Temperature-dependent EIS spectra were performed at 20, 30, 40, 50, and 60 °C, with 10 mV amplitude signal and a frequency sweep from 0.1 to 10^5 Hz.

In-situ EIS measurements were also performed using the Solartron electrochemical station, where charge/discharge tests were performed at a specific current of 0.1 A g^{-1}, and EIS spectra were collected at potentials spaced at 0.2 V intervals, with impedance tests performed at frequencies ranging from 0.1 to 10^5 Hz.

Distribution of relaxation time (DRT) curves were obtained by utilizing the DRTtools software, a MATLAB GUI for analyzing EIS data.

The EIS spectra were converted to a relaxation-based function $\gamma(ln\tau)$, where the peaks at a specific relaxation time τ (reciprocal of frequency, $1/f$ represent the relevant electrochemical process, and the peak area represents the impedance value. The DRT fitting results for AOH-VO, VEG, and AOH-VO-300 in the open circuit potential (Supplementary Fig. 34a–c).

GITT. Temperature-dependent diffusion coefficients of Zn^{2+} in solids were tested at 25, 40, and 55 °C by galvanostatic intermittent titration (GITT) technique for AOH-VO and VEG cathodes assembled to coin cells. Detail calculations can be found in Supplementary Note 7. Furthermore, we adopted an interpolated/extrapolated linear approximation to obtain diffusion coefficients at potential intervals of 0.025 V under different temperatures (Supplementary Fig. 31b). Then, the activation energies of Zn^{2+} diffusion in the solid framework under different potentials were calculated by the following equation:

$$D_{Zn} = D_{s0}e^{\frac{-E_{asf}}{k_BT}} \quad (7)$$

where D_{s0} is the pre-exponential factor in the solid, T is the operating temperature, and E_{asf} represents the diffusion activation energy in the solid framework.

Pouch cell. Detailed preparation procedures and component parameters for pouch cell is described in Supplementary Note 8 and Supplementary Table 8. The pouch cell was constructed with a double-layer structure, as shown in Supplementary Fig. 51. The AOH-VO was coated on Ti mesh (100 mesh, thickness: 0.27 mm, 9×10 cm^2) with carbon black and PVDF binders at a weight ratio of 7:2:1 (the AOH-VO mass loading of 37 mg cm^{-2}). The anode consisted of a 9 cm × 10 cm × 30 μm zinc foil with N-doped carbon nanofibers (NCNF) as an interlayer. The preparation of NCNF can also be found in Supplementary Note 8. 3 M $Zn(OTF)_2$ (12 ml) and glass fiber (93×103 cm^2) were used as the electrolyte and separator, respectively. The pouch cell, enclosed in a 10 cm × 11 cm × 0.2 cm Al packaging bag, underwent sealing using a hand-pressure sealer. All assembly procedures were conducted in an atmosphere at room temperature (~25 °C). Before cycling tests, the assembled pouch cells were allowed to stand for 12 h to ensure thorough wetting of the thick electrodes.

The electrochemical characterizations, long-term cycling, and rate performance tests of the Ah-level pouch cell were performed using a LANHE battery electrochemical tester G340A (Wuhan LAND Electronic Co. Ltd.), which can provide a total current of 40 A. This equipment offers higher accuracy, ensuring stable data collection even at large specific currents, operating within a potential window of 0.2–1.7 V (vs. Zn^{2+}/Zn). Long-term cycling tests were performed with rate-specific currents of 0.1 and 2 A/g, respectively. The specific capacity is calculated based on the cathode active material's mass, while the energy/power densities of the pouch cell are based on the weight of all components, excluding the Al soft packing films, see Supplementary Note 9 for detailed calculations. All electrochemical test experiments were performed at room temperature in an air environment.

Density functional theory calculations

All DFT calculations were performed by Perdew-Burke-Ernzerhof (PBE) generalized gradient approximation (GGA) exchange-correlation method, as implemented in the Vienna ab Initio Simulation Package (VASP). The projector augmented wave (PAW) method calculates the interaction between core and valence electrons. The cutoff energy of 340 eV and k-point separation of 0.04 Å were adopted in structural optimization. The convergence tolerance for the force and energy during relaxation was set to 0.05 eV $Å^{-1}$ and 10^{-5} eV, respectively. The diffusion of Zn^{2+} between VEG layers was simulated using the CI-NEB method. Because the naked Zn^{2+} and solvated Zn^{2+} possess the same charge and experience similar electrostatic repulsion from the host, we directly adopted the simplified model with naked Zn^{2+} to carry out DFT calculations.

Data availability

All data supporting this study and its findings are available within the article and its Supplementary Information (https://doi.org/10.6084/m9.figshare.27299616). The data corresponding to this study are available from the first author and corresponding authors upon request. Source data are also provided with this paper.

References

1. Wang, C.-Y. et al. Fast charging of energy-dense lithium-ion batteries. *Nature* **611**, 485–490 (2022).
2. Choi, C. et al. Achieving high energy density and high power density with pseudocapacitive materials. *Nat. Rev. Mater.* **5**, 5–19 (2019).
3. Liang, Y. & Yao, Y. Designing modern aqueous batteries. *Nat. Rev. Mater.* **8**, 109–122 (2022).
4. Li, C., Jin, S., Archer, L. A. & Nazar, L. F. Toward practical aqueous zinc-ion batteries for electrochemical energy storage. *Joule* **6**, 1727–1742 (2022).
5. Weiss, M. et al. Fast charging of lithium-ion batteries: a review of materials aspects. *Adv. Energy Mater.* **11**, 2101126 (2021).
6. He, X., Zhu, Y. & Mo, Y. Origin of fast ion diffusion in super-ionic conductors. *Nat. Commun.* **8**, 15893 (2017).
7. Wang, T. et al. Ultrafast 3D hybrid-Ion transport in porous V_2O_5 cathodes for superior-rate rechargeable aqueous zinc batteries. *Adv. Energy Mater.* **13**, 2204358 (2023).
8. Tang, B., Shan, L., Liang, S. & Zhou, J. Issues and opportunities facing aqueous zinc-ion batteries. *Energy Environ. Sci.* **12**, 3288–3304 (2019).
9. Jia, X., Liu, C., Neale, Z. G., Yang, J. & Cao, G. Active materials for aqueous zinc ion batteries: synthesis, crystal structure, morphology, and electrochemistry. *Chem. Rev.* **120**, 7795–7866 (2020).
10. Ruan, P., Liang, S., Lu, B., Fan, H. J. & Zhou, J. Design strategies for high-energy-density aqueous zinc batteries. *Angew. Chem. Int. Ed.* **61**, e202200598 (2022).
11. Qin, K., Huang, J., Holguin, K. & Luo, C. Recent advances in developing organic electrode materials for multivalent rechargeable batteries. *Energy Environ. Sci.* **13**, 3950–3992 (2020).
12. Huang, J. et al. Polyaniline-intercalated manganese dioxide nanolayers as a high-performance cathode material for an aqueous zinc-ion battery. *Nat. Commun.* **9**, 2906 (2018).
13. Ma, X. M. et al. Organic-inorganic hybrid cathode with dual energy-storage mechanism for ultrahigh-rate and ultralong-life aqueous zinc-ion batteries. *Adv. Mater.* **34**, e2105452 (2022).
14. Hong, S. et al. Efficient scalable hydrothermal synthesis of MnO_2 with controlled polymorphs and morphologies for enhanced battery cathodes. *ACS Energy Lett.* **8**, 1744–1751 (2023).
15. Wang, X. et al. 2D amorphous V_2O_5/graphene heterostructures for high-safety aqueous Zn-ion batteries with unprecedented capacity and ultrahigh rate capability. *Adv. Energy Mater.* **10**, 2000081 (2020).
16. Deng, S. et al. Electrochemically induced metal-organic-framework-derived amorphous V_2O_5 for superior rate aqueous zinc-ion batteries. *Angew. Chem. Int. Ed.* **59**, 22002–22006 (2020).
17. Whittingham, M. S. et al. The one dimensional chain structures of vanadyl glycolate and vanadyl acetate. *J. Mater. Chem.* **13**, 1420–1423 (2003).
18. Uchaker, E., Zhou, N., Li, Y. W. & Cao, G. Z. Polyol-mediated solvothermal synthesis and electrochemical performance of nanostructured V_2O_5 hollow microspheres. *J. Phys. Chem. C* **117**, 1621–1626 (2013).
19. Wang, X. R. et al. High-rate performance and ultralong cycle life enabled by hybrid organic-inorganic vanadyl ethylene glycolate for lithium-ion batteries. *Adv. Energy Mater.* **8**, 1801978 (2018).
20. Wong, J., Lytle, F. W., Messmer, R. P. & Maylotte, D. H. K-edge absorption spectra of selected vanadium compounds. *Phys. Rev. B Condens. Matter* **30**, 5596–5610 (1984).
21. Cezar, A. B., Graff, I. L., Varalda, J., Schreiner, W. H. & Mosca, D. H. Oxygen-vacancy-induced room-temperature magnetization in lamellar V_2O_5 thin films. *J. Appl. Phys.* **116**, 163904 (2014).
22. Liu, S. et al. Recent advances in vanadium-based aqueous rechargeable zinc-ion batteries. *Adv. Energy Mater.* **10**, 2000477 (2020).
23. Yuan, Y. et al. Understanding intercalation chemistry for sustainable aqueous zinc–manganese dioxide batteries. *Nat. Sustain.* **5**, 890–898 (2022).
24. Yang, X., Deng, W., Chen, M., Wang, Y. & Sun, C. F. Mass-producible, quasi-zero-strain, lattice-water-rich inorganic open-frameworks for ultrafast-charging and long-cycling zinc-ion batteries. *Adv. Mater.* **32**, e2003592 (2020).
25. Wang, L. L., Huang, K. W., Chen, J. T. & Zheng, J. R. Ultralong cycle stability of aqueous zinc-ion batteries with zinc vanadium oxide cathodes. *Sci. Adv.* **5**, eaax4279 (2019).
26. Oberholzer, P., Tervoort, E., Bouzid, A., Pasquarello, A. & Kundu, D. Oxide versus nonoxide cathode materials for aqueous Zn batteries: an insight into the charge storage mechanism and consequences thereof. *ACS Appl. Mater. Interfaces* **11**, 674–682 (2019).
27. Wang, L. L. et al. Ultrahigh-rate and ultralong-life aqueous batteries enabled by special pair-dancing proton transfer. *Sci. Adv.* **9**, eadf4589 (2023).
28. Zhu, K., Wu, T., van den Bergh, W., Stefik, M. & Huang, K. Reversible molecular and ionic storage mechanisms in high-performance $Zn_{0.1}V_2O_5{\cdot}nH_2O$ xerogel cathode for aqueous Zn-ion batteries. *ACS Nano* **15**, 10678–10688 (2021).
29. Dai, Y. H. et al. Quicker and more Zn^{2+} storage predominantly from the interface. *Adv. Mater.* **33**, e2100359 (2021).
30. Augustyn, V. et al. High-rate electrochemical energy storage through Li^+ intercalation pseudocapacitance. *Nat. Mater.* **12**, 518–522 (2013).
31. Liu, N. N. et al. Intercalation pseudocapacitive Zn^{2+} storage with hydrated vanadium dioxide toward ultrahigh rate performance. *Adv. Mater.* **32**, e1908420 (2020).
32. Ding, J. W. et al. Ultrafast Zn^{2+} intercalation and deintercalation in vanadium dioxide. *Adv. Mater.* **30**, 1800762 (2018).
33. Wang, X. et al. Pseudocapacitive zinc cation intercalation with superior kinetics enabled by atomically thin V_2O_5 Nanobelts for quasi-solid-state microbatteries. *Energy Stor. Mater.* **50**, 454–463 (2022).
34. Zhang, Q. et al. Modulating electrolyte structure for ultralow temperature aqueous zinc batteries. *Nat. Commun.* **11**, 4463 (2020).
35. Song, Z. Y. et al. Proton-conductive supramolecular hydrogen-bonded organic superstructures for high-performance zinc-organic batteries. *Angew. Chem. Int. Ed.* **62**, e202219136 (2023).
36. Li, W. et al. Tuning electron delocalization of hydrogen-bonded organic framework cathode for high-performance zinc-organic batteries. *Nat. Commun.* **14**, 5235 (2023).
37. Xia, C. et al. Rechargeable aqueous zinc-ion battery based on porous framework zinc pyrovanadate intercalation cathode. *Adv. Mater.* **30**, 1705580 (2018).
38. Zhu, K., Wu, T. & Huang, K. $NaCa_{0.6}V_6O_{16}{\cdot}3H_2O$ as an ultra-stable cathode for Zn-ion batteries: the roles of pre-inserted dual-cations and structural water in V_3O_8 layer. *Adv. Energy Mater.* **9**, 1901968 (2019).
39. Hu, L. F. et al. Principles of interlayer-spacing regulation of layered vanadium phosphates for superior zinc-ion batteries. *Energy Environ. Sci.* **14**, 4095–4106 (2021).
40. Huang, J. et al. In situ induced coordination between a "Desiccant" interphase and oxygen-deficient navajoite towards highly efficient zinc ion storage. *Adv. Energy Mater.* **12**, 2201434 (2022).
41. Liu, S. C. et al. Tuning the kinetics of zinc-ion insertion/extraction in V_2O_5 by in situ polyaniline intercalation enables improved aqueous zinc-ion storage performance. *Adv. Mater.* **32**, e2001113 (2020).

42. Nam, K. W. et al. Conductive 2D metal-organic framework for high-performance cathodes in aqueous rechargeable zinc batteries. *Nat. Commun.* **10**, 4948 (2019).
43. Kundu, D. et al. Aqueous vs. nonaqueous Zn-ion batteries: consequences of the desolvation penalty at the interface. *Energy Environ. Sci.* **11**, 881–892 (2018).
44. Xu, C. J., Li, B. H., Du, H. D. & Kang, F. Y. Energetic zinc ion chemistry: the rechargeable zinc ion battery. *Angew. Chem. Int. Ed.* **51**, 933–935 (2012).
45. Alfaruqi, M. H. et al. A layered δ-MnO_2 nanoflake cathode with high zinc-storage capacities for eco-friendly battery applications. *Electrochem. Commun.* **60**, 121–125 (2015).
46. Lin, T. Q. et al. Nitrogen-doped mesoporous carbon of extraordinary capacitance for electrochemical energy storage. *Science* **350**, 1508–1513 (2015).
47. Wan, F. et al. A universal compensation strategy to anchor polar organic molecules in bilayered hydrated vanadates for promoting aqueous zinc-ion storage. *Adv. Mater.* **33**, 2102701 (2021).
48. Zhao, Y. et al. Achieving high capacity and long life of aqueous rechargeable zinc battery by using nanoporous-carbon-supported poly(1,5-naphthalenediamine) nanorods as cathode. *Energy Storage Mater.* **28**, 64–72 (2020).
49. Fei, B. et al. In situ induced core-shell carbon-encapsulated amorphous vanadium oxide for ultra-long cycle life aqueous zinc-ion batteries. *Adv. Funct. Mater.* **33**, 2215170 (2023).
50. Sun, H. T. et al. Three-dimensional holey-graphene/niobia composite architectures for ultrahigh-rate energy storage. *Science* **356**, 599–604 (2017).
51. Liu, M. et al. Synchronous-ultrahigh conductive-reactive N-atoms doping strategy of carbon nanofibers networks for high-performance flexible energy storage. *Energy Storage Mater.* **44**, 250–262 (2022).
52. Li, Y. et al. A bifunctional nitrogen doped carbon network as the interlayer for dendrite-free Zn anode. *Chem. Eng. J.* **452**, 139264 (2023).
53. Jiang, L., Dong, D. & Lu, Y.-C. Design strategies for low temperature aqueous electrolytes. *Nano Res. Energy* **1**, e9120003 (2022).

Acknowledgements

This work was financially supported by the National Natural Science Foundation of China (Nos. 51972051, 52072064, 62171115, 52332004), the Natural Science Foundation of Jilin Province of China (20220101219JC), and the funding from Jilin Province (No. 20220502002GH). The authors sincerely acknowledge Dr. Hancheng Zhu and Dr. Guorui Wang for providing technology supporting the characterization of the samples.

Author contributions

M.Z.L. and X.H.L. designed and conducted the experiments, performed the electrochemical and characterization tests, and analyzed the data. X.H.L. and M.X.C. performed the DFT simulations. M.Z.L., X.H.L. and C.L.S. organized and wrote the manuscript. M.Z.L., F.Y.C., J.X.L., W.J.S. and Y.L. contributed to the structural characterizations and electrochemical measurements. Y.W. and W.Z. contributed to the spherical aberration-corrected microscope test. X.H.L., X.W.L., C.L.S. and Y.C.L. supervised the project. All authors contributed to the discussion and revision of the manuscript.

Competing interests

The authors declare no competing interests.

Additional information

Supplementary information The online version contains supplementary material available at https://doi.org/10.1038/s41467-024-55000-8.

Correspondence and requests for materials should be addressed to Xinghua Li, Changlu Shao or Yichun Liu.

Peer review information *Nature Communications* thanks Shuquan Liang, Xiaowei Wang and the other, anonymous, reviewer(s) for their contribution to the peer review of this work. A peer review file is available.